ELSEVIER

Journal of Quantitative Spectroscopy & Radiative Transfer 93 (2005) 231–243

Journal of Quantitative Spectroscopy & Radiative Transfer

www.elsevier.com/locate/jqsrt

Simulation of whispering-gallery-mode resonance shifts for optical miniature biosensors

Haiyong Quan, Zhixiong Guo*

Department of Mechanical and Aerospace Engineering, Rutgers, The State University of New Jersey, 98 Brett Road, Piscataway, NJ 08854, USA

Received 1 February 2004; accepted 1 July 2004

Abstract

Finite element analyses are made of the shifts of resonance frequencies of whispering-gallery-mode (WGM) for a fiber–microsphere coupling miniature sensor. The time-domain Maxwell's equations were adopted to describe the near-field radiation transport and solved by the in-plane TE waves application mode of the FEMLAB. The electromagnetic fields as well as the radiation energy distributions can be easily obtained by the finite element analysis. The resonance intensity spectrum curves in the frequency range from 213 to 220 THz were studied under different biosensing conditions. Emphasis was put on the analyses of resonance shift sensitivity influenced by changes of the effective size of the sensor resonator (i.e., microsphere) and/or the refractive index of the medium surrounding the resonator. It is estimated that the WGM biosensor can distinguish molecular size change to the level of 0.1 nm and refractive index change in the magnitude of $\sim 10^{-3}$ even with the use of a general optical spectrum analyzer of one GHz linewidth. Finally, the potential of the WGM miniature biosensor for monitoring peptide growth is investigated and a linear sensor curve is obtained.

Keywords: Whispering-gallery-mode resonance; Near-field radiation transport; Optical frequency shift spectrum; Miniature sensor; Nanoscopic biosensing; Peptide growth monitoring; Finite element analysis

*Corresponding author. Tel.: +1-732-445-2024; fax: +1-732-445-3124.
E-mail address: guo@jove.rutgers.edu (Z. Guo).

0022-4073/$ - see front matter © 2004 Elsevier Ltd. All rights reserved.
doi:10.1016/j.jqsrt.2004.08.023

1. Introduction

In recent years, the advances in micro/nano-fabrication techniques have made it feasible to consider optical resonators having physical dimensions of the order of optical wavelength. As a particular mode of microcavity resonances, the whispering-gallery-mode (WGM) is a morphology-dependent resonance. WGM occurs when light travels in a dielectric medium of circular geometries. After repeated total internal reflections at the curved boundary, the electromagnetic field can close on itself and give rise to resonances. If the dielectric medium is a microsphere, one obtains a very small mode volume and high finesse. In order to couple light in or out of the microsphere, it is necessary to utilize overlapping of the evanescent radiation field of WGMs with the evanescent field of a phase-matched optical fiber or waveguide. Photons tunnel from the eroded optical fiber to the microsphere if their refractive indices are very close.

The WGM resonance phenomenon has recently received increasing attention due to their high potential for the realization of microlasers [1,2], narrow filters [3], optical switching [4], miniature biosensors [5], high-resolution spectroscopy [6], etc. Examples of the high potential applications of WGM biosensors include identification and monitoring of proteins, DNA, peptides, and toxin molecules. WGM biosensors can have very compact configuration and high sensibility for molecular probing. They can detect as few as 100 molecules [5]. Blair and Chen [7] studied resonance-enhanced evanescent-wave fluorescence biosensing of the binding of a labeled analyte with a biospecific monolayer. They showed the improvement in sensitivity by over an order of magnitude and sample volume reduction by many orders of magnitude. Arnold's research group [8,9] investigated protein adsorption biosensors using WGMs. They used perturbation approach [10] to analyze the resonance shifts and predicted that the shift should be inversely proportional to the microsphere radius and proportional to protein surface density and excess polarizability.

In WGM resonators an interesting phenomenon is that the resonance peaks in the light intensity spectrum curve is very sharp and the intervals between two successive peaks are very stable. Moreover, the resonance frequencies will shift with the changes of the microsphere size and/or the optical properties of the surrounding medium. These properties can be applied for the detection of bio-molecules. Adsorption of different kinds of molecules on the surface of the microsphere of WGM sensors results in changes of the effective microsphere size and/or the optical properties of the surrounding medium, and leads to shifts of resonance frequencies. In order to detect a specific molecule sensitively, the corresponding sensor configurations, such as the excitation laser tunable range, the microsphere size, the gap between the microsphere and waveguide, and the refractive index of the materials, need to be designed and optimized. The experimental method to optimize those parameters is very costly. A flexible simulation model is highly desired.

In this paper, we investigate the feasibility and sensitivity in the detection and monitoring of peptide growth and/or adsorption using a fiber–microsphere coupling WGM miniature biosensor. The coupling of fiber–microsphere has several advantages. For example, such kinds of sensors can be relatively easily made in labs, and ideal matching to the WGMs of the sphere is possible [10]. Typical resonance inside a microsphere is an equatorial brilliant ring, and this ring is located on the same plane as the tapered fiber line. So it is feasible to use a two-dimensional (2-D) theoretical model. The Lorenz–Mie theory [11] and the first-order perturbation model [10] were commonly used for analytical studies. A variety of numerical methods were also considered for modeling the

WGMs. The most widely used numerical model is the finite-difference time-domain (FDTD) method [12]. The drawbacks of the FDTD method lie with the time consuming in obtaining stationary solutions, the large memory requirement, and the difficulty in the treatment of irregular configurations. Here, we use the finite element method (FEM) to solve the time-domain Maxwell's equations. The shifts of the resonance frequencies and the quality factor Q were obtained through the analyses of intensity spectrum curves. The simulation model can predict the electromagnetic field and the evanescent radiation field (Poynting's vector). It is very convenient and powerful for optimal design of WGM resonators. Using this simulation model, we calculated the sensor curve for measuring and monitoring the growth of peptides in solid-phase synthesis.

2. Mathematical formulation

The time-dependent Maxwell's equations are

$$\nabla\cdot\bar{E}=\frac{\rho}{\varepsilon},\quad \nabla\times\bar{E}=-\mu\frac{\partial\bar{H}}{\partial t},$$
$$\nabla\cdot\bar{H}=0,\quad \nabla\times\bar{H}=\bar{J}+\varepsilon\frac{\partial\bar{E}}{\partial t}, \tag{1}$$

where $\bar{E}$ and $\bar{H}$ are the electric and magnetic field vectors, respectively; ε and μ are the permittivity and permeability of the medium; ρ is the electric charge density; and $\bar{J}$ is the electric current density.

For the electric field, since $\rho=0$ and $\bar{J}=\sigma\bar{E}$, we can derive the equation for $\bar{E}$ as follows:

$$\nabla^2\bar{E}-\mu\sigma\frac{\partial\bar{E}}{\partial t}-\mu\varepsilon\frac{\partial^2\bar{E}}{\partial t^2}=0, \tag{2}$$

where σ is the electrical conductivity. We can transfer the above equation to the form of a time-harmonic wave by setting $\bar{E}(\bar{r},t)=\bar{E}_0(\bar{r})\mathrm{e}^{\mathrm{i}\omega t}$. The coupled set of Maxwell's equations can be reduced to the following simple form:

$$\frac{1}{\mu}\nabla^2\bar{E}+\omega^2\varepsilon_{\mathrm{c}}\bar{E}=0, \tag{3}$$

where we have introduced the complex permittivity $\varepsilon_{\mathrm{c}}=\varepsilon-\mathrm{i}(\sigma/\omega)$ and $\omega=2\pi c/\lambda$; and c is the speed of light in the medium and λ is the light wavelength. Here, the complex index of refraction, $m=n-\mathrm{i}k$, is conveniently introduced for the treatment of wave propagation; n is the real part of the refractive index and represents a spatial-phase change of the electromagnetic wave; k is the absorption index and stands for a spatial damping on the electromagnetic wave [13,14]. The relationship between ε_{c} and m is expressed by $\varepsilon_{\mathrm{c}}=m^2=n^2-k^2-\mathrm{i}2nk$.

Similarly, we can obtain an equation for $\bar{H}$:

$$\frac{1}{\mu}\nabla^2\bar{H}+\omega^2\varepsilon_{\mathrm{c}}\bar{H}=0. \tag{4}$$

In the present study we apply the in-plane TE waves application mode, where the electric field vector has only a z-component; and it propagates in the modeling x–y plane. Thus, the fields can

be written as

$$\tilde{E}(x,y,t) = E_z(x,y)\bar{e}_z e^{i\omega t}, \tag{5}$$

$$\tilde{H}(x,y,t) = [H_x(x,y)\bar{e}_x + H_y(x,y)\bar{e}_y]e^{i\omega t}. \tag{6}$$

To get a full description of the electromagnetic problem, we also need to specify the boundary conditions. At the interface and physical boundaries, we used the natural continuity condition for the tangential component of the magnetic field:

$$\bar{n} \times \tilde{H} = 0. \tag{7}$$

For the outside boundaries, the low-reflecting boundary condition is adopted. The low-reflecting means that only a small part of the wave is reflected, and that the wave propagates through the boundary almost as if it were not present. This condition can be formulized as

$$\bar{e}_z \cdot \bar{n} \times \sqrt{\mu}\tilde{H} + \sqrt{\varepsilon}E_z = 0. \tag{8}$$

The laser source term E_{0z}, which propagates inwards through the outside boundary of the fiber, was treated as the electric, low-reflecting boundary condition and expressed by

$$E_{0z} = \frac{1}{2\sqrt{\varepsilon}}(\bar{e}_z \cdot \bar{n} \times \sqrt{\mu}\tilde{H} + \sqrt{\varepsilon}E_z). \tag{9}$$

The WGM resonances possess very high-quality factors due to minimal reflection losses. The quality factor Q is defined as a ratio of 2π stored energy to energy lost per cycle. From the energy conservation and resonance properties, we can deduce a simple approximate expression [11,15]:

$$Q = \omega_0/\Delta\omega = 2\pi\omega_0\tau, \tag{10}$$

where ω_0 is the resonant frequency, $\Delta\omega$ is the resonance linewidth, and τ is the photon lifetime.

3. Simulation model and method

The schematic of the WGM biosensor is shown in Fig. 1, where the simulation domain is a $35\,\mu m \times 40\,\mu m$ rectangular area meshed by 53,000 triangle elements. The in-plane TE waves application mode of the commercial software package FEMLAB was employed for the finite element analysis. In order to solve the problem using the FEM, we need to convert the foregoing strong formulation to a weak form. By applying the Galerkin method to Eq. (3), the integral form of the equation is obtained as

$$\int_\Omega W \cdot \left(\frac{1}{\mu}\nabla^2\Phi + \omega^2\varepsilon_c\Phi\right) d\Omega = 0, \tag{11}$$

where Φ is a set of trial function (approximation of E_Z) that satisfies the boundary conditions, W is a weighting or test function, and Ω is the computational domain. Integrating the first term of Eq. (11) by parts results in

$$\int_\Omega \left(\frac{1}{\mu}\nabla W \cdot \nabla\Phi - \omega^2\varepsilon_c W \cdot \Phi\right) d\Omega - \oint_\Gamma \frac{1}{\mu} W \frac{d\Phi}{dn} d\Gamma = 0, \tag{12}$$

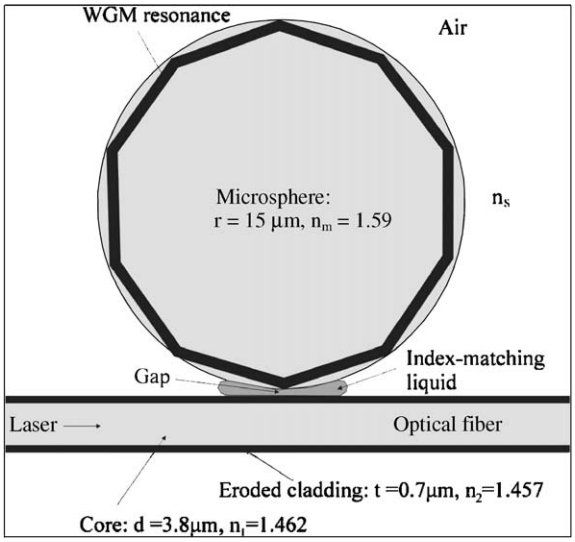

Fig. 1. The simulation model.

where Γ is the boundary of the domain. Now we use the basic shape function $N(x, y)$ to expand Φ and W:

$$\Phi = \sum_{i=1}^{n} N_i E_{Zi}, \tag{13}$$

$$E'_Z = \frac{\mathrm{d}\Phi}{\mathrm{d}n} = \sum N_i E'_{Zi}, \tag{14}$$

$$W = \sum_{i=1}^{n} N_i. \tag{15}$$

Here, n is the number of nodes and subscript i represents the node order. The numerical discretization is completed with the enforcement of Eq. (12) for all finite elements. Substituting Eqs. (13)–(15) into Eq. (12) results in the following matrix formation:

$$[S][E_Z] - [T][E'_Z] = 0 \tag{16}$$

with

$$[S] = \sum_{\text{all-element}} \int_{\Omega_e} \left(\frac{1}{\mu} \nabla N^{\mathrm{T}} \cdot \nabla N - \omega^2 \varepsilon_{\mathrm{c}} N^{\mathrm{T}} \cdot N \right) \mathrm{d}\Omega, \tag{17}$$

$$[T] = \sum_{\text{all-boundary-elements}} \int_{\Gamma_e} \frac{1}{\mu} N^{\mathrm{T}} \cdot N \, \mathrm{d}\Gamma, \tag{18}$$

where N is a row vector, $\{N_1, N_2, \ldots\}$, and N^{T} is a transpose vector of N. The line integral in Eq. (18) needs to be evaluated only over elements that have a side in common with the boundaries of the problem. Normally this integral is simply set to zero, which gives the so-called natural

boundary condition. The basis of polynomial functions $N(x, y)$ gives an approximation of the solution into the element.

Each simulation only took about 5 min in a DELL PC with one 2.0 GHz CPU. In general simulations, the microsphere is made from polystyrene or silica glass and is assumed to have a refractive index of $n_m = 1.59$. The diameter of the microsphere is 30 μm. The single-mode optical fiber with a core radius of 1.9 μm (refractive index $n_1 = 1.462$) and a cladding radius of 2.6 μm (refractive index $n_2 = 1.457$) is coupled with the microsphere. The microsphere is the probing head of the miniature biosensor. The coupling gap between the fiber and the microsphere is 5 nm. The surrounding medium is assumed to be air in the present study, but it can be any bio-solutions. A small amount of index-matching liquid is dipped in a small region of the narrow gap. The cladding of the fiber is eroded in the segment across the microsphere such that the cladding thickness in the whole simulation model is only 0.7 μm. A tunable continuous-wave laser is incident from the left end, and the light is confined in the single-mode fiber. The frequency of the incident laser varies between 213–220 THz. The general computational resolution of wavelength is 1 nm, but special attention is paid to the resonance frequencies where 0.1 nm resolution is employed. When protein, peptide, or DNA molecules are adsorbed on the surface of the microsphere, the resonance frequency will slightly shift [9]. The deposition of the molecules may affect the WGM resonance in two aspects: (1) it increases the effective size of the microsphere, i.e., the propagation pathway of the photons inside the microsphere increases; and/or (2) it changes the contrast of refractive indices between the microsphere and its surrounding medium.

4. Results and discussion

First, we calculated the electromagnetic fields and radiation energy fields of the WGM biosensor for given excitation laser frequencies in the range from 213 to 220 THz. Figs. 2, 3, and 4

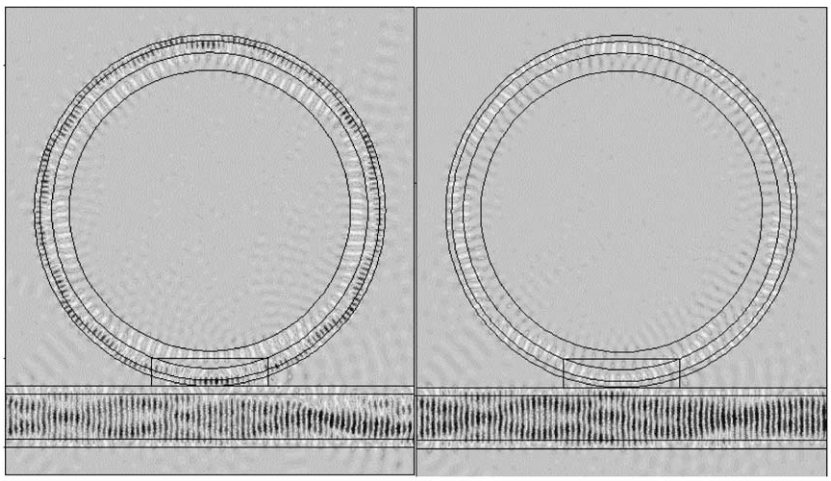

Fig. 2. The electric field distributions of the sensor: (a) on-resonance and (b) off-resonance.

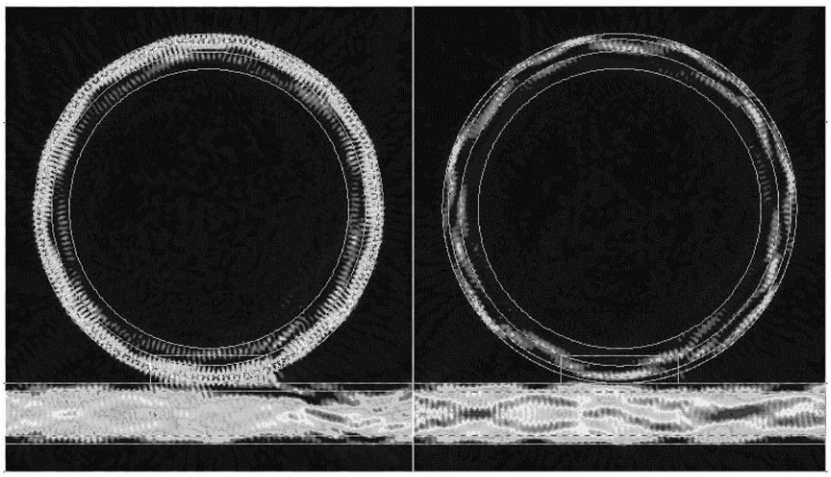

(a) (b)

Fig. 3. The norm electric field distributions of the sensor: (a) on-resonance and (b) off-resonance.

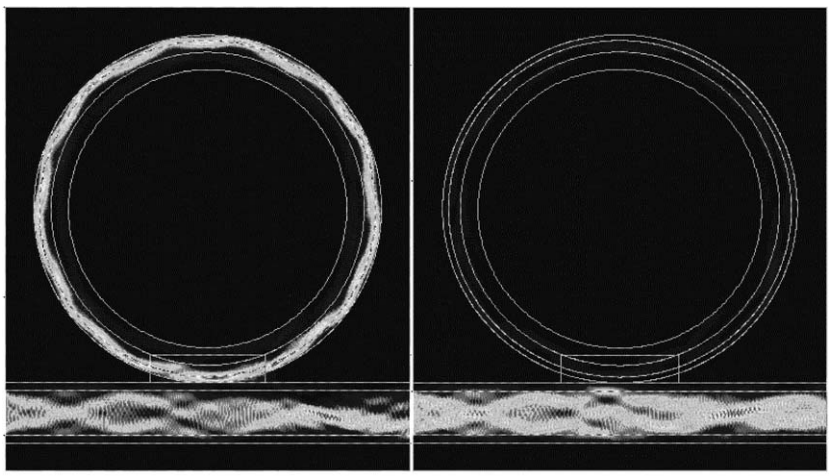

(a) (b)

Fig. 4. The energy flow distributions of the sensor: (a) on-resonance and (b) off-resonance.

display the distributions of the electric field, norm electric field, and Poynting's vector, respectively, in which the characteristics of the distributions on resonance and off-resonance frequencies are visualized. The resonance frequency was 219.2 THz ($\lambda = 1368.5$ nm) and the off-resonance one was 218.3 THz ($\lambda = 1374$ nm). The diameter of WGM sensor microsphere was 30 μm and the refractive index of the surrounding medium was 1.0. The norm electric field $|\bar{E}|$ usually represents the energy intensity ($|\bar{E}|^2$) in electromagnetism. The Poynting's vector stands for the energy flow, and is convenient for describing the radiation propagation property of the WGM biosensor. From these three figures, it is seen that photon tunneling phenomenon [16] is very obvious at resonance frequency. Exceedingly bright rings around the inside circle of the

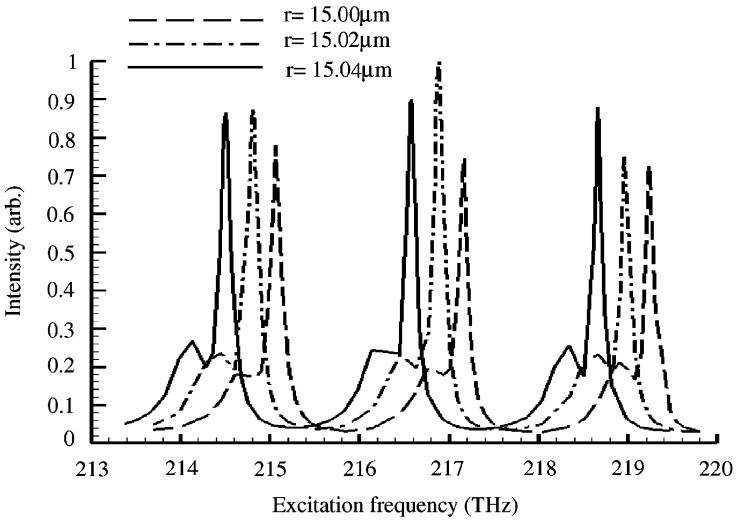

Fig. 5. Scattering spectra for different sizes of the microsphere: $r = 15\,\mu m$, $15.02\,\mu m$, and $15.04\,\mu m$, respectively.

microsphere surface are found, whereas the electric field and energy intensity in the surrounding medium are hardly visible. Photons were well confined inside the microsphere and total internal reflection occurred. At off-resonance frequency, photons still tunnel from the fiber to the microsphere. However, the strength of the electric field and energy flow field is extremely weak as compared to the resonance case. The ratio of the radiation intensity storing in the microsphere to the radiation intensity passing through the fiber is 1.8 at resonance in Fig. 4a, whereas it is only 0.044 at off-resonance in Fig. 4b. The microsphere can absorb and store the majority of the radiation energy when WGM resonance occurs. This leads to the enhancement of resonant radiation field inside the microsphere.

To investigate the influences of the effective microsphere size change and the variation of refractive index in the surrounding medium, we obtained the scattering[1] spectra [9] of radiation energy outflow from the microsphere surface with varying excitation frequencies between 213 and 220 THz for different microsphere sizes and refractive indices. Fig. 5 shows the radiation intensity spectrum curves for three different microsphere sizes. The surrounding medium was air. The increase of the microsphere size represents the adsorption or attachment of molecules. It is seen that the resonance frequency will shift to the left with the increase of the microsphere radius. This shift phenomenon can be explained by the optical resonance principle. The enlargement of the microsphere size results in the increment of the effective traveling distance of photons in the microsphere. Accordingly, it requires a longer wavelength to match the resonance condition under the same resonance mode. Therefore, the resonance frequency will decrease.

Fig. 6 portrays the radiation intensity spectrum curves for three different refractive indices of the surrounding medium. The diameter of the microsphere is fixed at 30 μm. It is clearly observed that the resonance frequency will shift to the decrescent direction with increase of the refractive index. This shift tendency results from the change of the critical angle of total internal reflection.

[1]This scattering intensity of the microsphere is roughly proportional to its intracavity energy. The resonance phenomenon can be found by monitoring it.

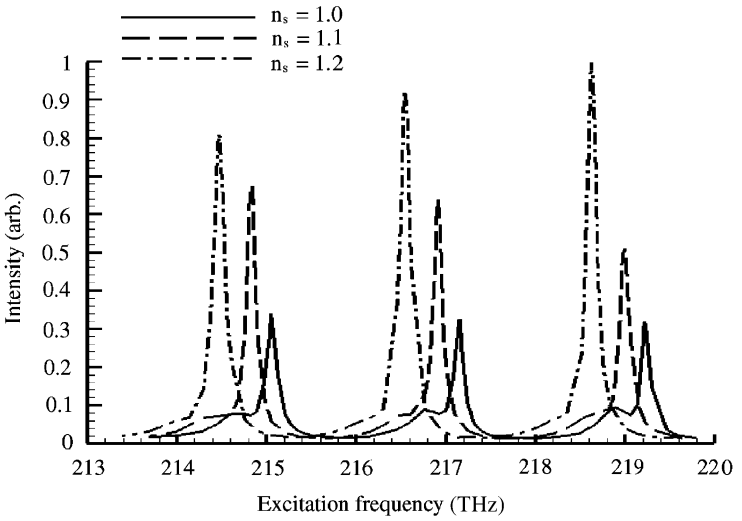

Fig. 6. Scattering spectra for different refractive indices of the surrounding medium: $n_s = 1.0$, 1.1, and 1.2, respectively.

From the critical angle expression, $\theta_c = \sin^{-1}(n_s/n_m)$, θ_c will increase with the increase of n_s. This results in increase of the effective traveling distance of the photons in a resonance mode and requires the light with a longer wavelength to match the resonance condition in order to keep the same resonance mode. Therefore, the resonance frequency will decrease.

Tables 1 and 2 list the resonance property data analyzed from the radiation spectra in Figs. 5 and 6. In Table 1, the resonance frequencies and corresponding wavelengths, the quality factors, and the resonance frequency intervals are presented. Three resonance frequencies were found in the frequency range considered. The quality factors of these resonance modes are varying between 1430 and 1830. The resonance frequency intervals are slightly varying between 2.06 and 2.10 THz. The calculation resolution at resonance frequencies was 0.1 nm. We can estimate that the accuracy of the calculated resonance frequency is ± 0.02 THz.

Table 2 lists the frequency shifts with respect to the change of either the microsphere size or the refractive index of the surrounding medium. It is found that with the increase of either the microsphere size or the surrounding medium refractive index, the resonance frequency always shifts to the decrescent direction. The response to an increase of 20 nm in the microsphere radius is a significant resonance frequency downshift of 0.27 THz in average for the three resonance modes. While an increase of 40 nm results in an average downshift of 0.56 THz. Such shifts are substantial. Since the current state-of-the-art optical instrument can reach to a fine linewidth of ~ 10 MHz, the sensitivity of the WGM biosensor against the adsorption or attachment of molecules is then estimated in the magnitude of $\sim 10^{-3}$ nm. In other words, this sensor could detect minute adsorption, attachment, or growth of molecules on the surface of the microsphere in the order of $\sim 10^{-3}$ nm. Even with a rough linewidth of 1 GHz, the sensitivity can still reach to 0.1 nm.

This type of biosensor can also measure minute variation in the refractive index of the surrounding medium. In Table 2, the average downshift of the three resonance modes is 0.24 THz

Table 1
Resonance data from the radiation spectra

Resonance frequency f_R (THz)	Excitation Wavelength λ_R (nm)	Quality factor Q	Resonance frequency interval Δf (THz)
$n_s = 1.0$, $r = 15.00\,\mu m$			
215.054	1395.0	1434	2.101
217.155	1381.5	1448	2.063
219.218	1368.5	1462	
$n_s = 1.1$, $r = 15.00\,\mu m$			
214.823	1396.5	1790	2.081
216.904	1383.1	1808	2.074
218.978	1370.0	1825	
$n_s = 1.2$, $r = 15.00\,\mu m$			
214.454	1398.9	1532	2.090
216.544	1385.4	1547	2.067
218.611	1372.3	1562	
$n_s = 1.0$, $r = 15.02\,\mu m$			
214.792	1396.7	1432	2.081
216.873	1383.3	1446	2.073
218.946	1370.2	1460	
$n_s = 1.0$, $r = 15.04\,\mu m$			
214.500	1398.6	1430	2.075
216.575	1385.2	1445	2.089
218.664	1371.97	1458	

Table 2
Frequency shift data

Frequency shift (THz) Resonance frequency (THz)	$n_s = 1.0$	$n_s = 1.1$	$n_s = 1.2$
215.054	0	−0.231	−0.600
217.155	0	−0.251	−0.611
219.218	0	−0.240	−0.607
Resonance frequency (THz)	$r = 15.00\,\mu m$	$r = 15.02\,\mu m$	$R = 15.04\,\mu m$
215.054	0	−0.262	−0.554
217.155	0	−0.282	−0.580
219.218	0	−0.272	−0.554

for a refractive index change of 0.1 and 0.61 THz for a refractive index change of 0.2, respectively. It is estimated that a minute variation of the surrounding medium refractive index in the order of $\sim 10^{-5}$ is distinguishable by this WGM biosensor when a linewidth of ~ 10 MHz is considered.

Such high sensitivities make the WGM sensors feasible for potential applications for identifying the physical properties of molecules of DNA, proteins, and peptides, and monitoring the processes of molecular interactions.

Finally, we show an example of the potential application in the monitoring of peptide growth. The method of solid phase peptide synthesis (SPPS) was invented by Bruce Merrified [17]. Nowadays SPPS dominates in the synthesis of peptides. In the synthetic procedure, polystyrene microparticle beads are applied as polymer supports, and certain amino acids are covalently bound to polymer supports via the polyethylene glycol linkers and then grow on the surfaces of the polymer supports to fashion peptide chains. The conformation of a peptides chain may be an α-helix, β-sheet, or other arrangements. Monitoring and controlling the growth thickness of peptides is very important for peptide synthesis to control the quality and cost.

Fig. 7 shows the sensor curve for measuring and monitoring the growth thickness of peptides. The fiber–microsphere WGM biosensor has a polystyrene microbead of 30 μm in diameter. The WGM resonance mode is operated at the frequency of 217.155 THz. When peptides grow, the resonance frequency downshifts. The thicker is the peptide layer, the larger is the resonance frequency shift. In general, the thickness of one-layer peptide is about 0.34 nm. Here, we simply treat the thickness of every three peptide layers as 1 nm. In Fig. 7, 11 data are shown for peptide thickness in the range from 0–10 nm (i.e., up to 30 layers) with an increment of 1 nm. We found a linear relationship between the peptide thickness and the absolute value of the downshift of resonance frequency. Using the best-fitting technique, the sensor curve equation is obtained: $\Delta f = -13.98091\Delta r - 0.813636$ (GHz), where Δf and Δr are the resonance frequency shift and peptide thickness, respectively. The correlation coefficient of the linearity is 0.999. Considering that the linear characteristic is a fundamental requirement for an ideal biosensor, the results show the feasibility of the WGM biosensor as an excellent miniature biosensor in the monitoring of peptide growth and synthesis.

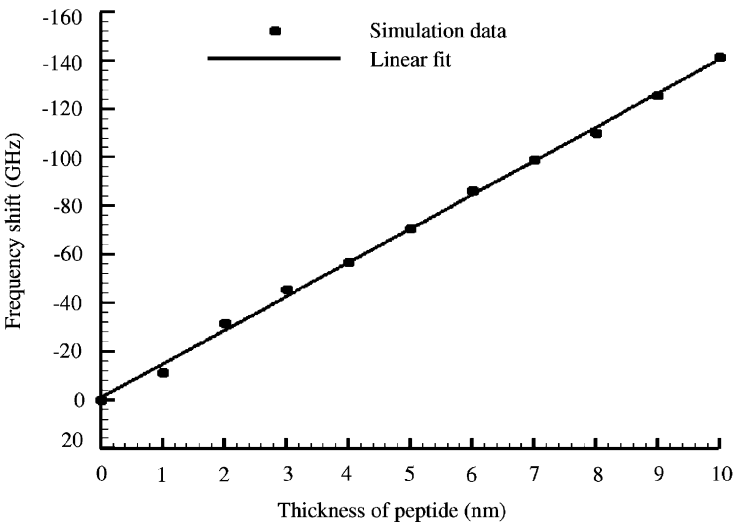

Fig. 7. Sensor curve of the WGM biosensor for the monitoring of peptide growth.

5. Conclusions

The characteristics of a fiber–microsphere coupling WGM miniature biosensor are studied numerically. The electromagnetic and radiation fields are obtained by solving the time-domain Maxwell's equations using the finite element analysis. It is found that the increase of either the effective microsphere size or the refractive index of the medium surrounding the microsphere down-shifts the WGM resonance frequency. The larger the change, the stronger the shift is. A linear relationship between the variation of microsphere effective size and the resonance frequency shift is found. This characteristic may be used for the monitoring of peptide growth in the solid-phase synthesis. The WGM biosensor can measure the adsorption or growth of one single peptide layer. If the optical instrument reaches a resolution of $\sim 10\,\mathrm{MHz}$, the sensitivity of the WGM biosensor is estimated in the magnitude of $\sim 10^{-3}\,\mathrm{nm}$ for the detection of adsorption or attachment of molecules on the microsphere and in the magnitude of $\sim 10^{-5}$ for the detection of refractive index change in the surrounding medium. Such high sensitivities picture prosperous potentials of WGM miniature biosensors in the applications in drug discovery, DNA detection, peptide monitoring, protein identification, etc. Specifically, we proposed for the first time the monitoring of peptide growth using WGM miniature biosensors.

Acknowledgements

Z. Guo acknowledges the support of a 2003–2004 Academic Excellence Fund Award from Rutgers University, and an NSF Grant (CTS-0318001). Helpful discussion concerning peptide synthesis and growth monitoring with Dr. M.G. Shiue, the president of Princeton Biomolecules Corporation, is highly appreciated.

References

[1] Cai M, Painter O, Vahala KJ, Sercel PC. Fiber-coupled microsphere laser. Opt Lett 2000;25:1430–2.
[2] Cai M, Vahala K. Highly efficient hybrid fiber coupled microsphere laser. Opt Lett 2001;26:884–6.
[3] Little BE, Chu ST, Haus HA, Foresi J, Laine J-P. Microring resonator channel dropping filters. J Lightwave Tech 1997;15:998–1005.
[4] Blom FC, Van Dijk DR, Hoekstra HJ, Driessen A, Popma ThJA. Experimental study of integrated-optics micro-cavity resonators: toward an all-optical switching device. Appl Phys Lett 1997;71:747–9.
[5] Boyd RW, Heebner JE. Sensitive disk resonator photonic biosensor. Appl Opt 2001;40:5742–7.
[6] Schiller S, Byer RL. High-resolution spectroscope of whispering gallery modes in large dielectric spheres. Opt Lett 1991;16:1138–40.
[7] Blair S, Chen Y. Resonant-enhanced evanescent-wave fluorescence biosensing with cylindrical optical cavities. Appl Opt 2001;40:570–82.
[8] Vollmer F, Braun D, Libchaber A, Khoshsima M, Teraoka I, Arnold S. Protein detection by optical shift of a resonant microcavity. Appl Phys Lett 2002;80:4057–9.
[9] Arnold S, Khoshsima M, Teraoka I, Vollmer F. Shift of whispering-gallery modes in microspheres by protein adsorption. Opt Lett 2003;28:272–4.
[10] Teraoka I, Arnold S, Vollmer F. Perturbation approach to resonance shifts of whispering-gallery modes in a dielectric microsphere as probe of a surrounding medium. J Opt Soc Am B 2003;20:1937–46.

[11] Barber PW, Chang PK. Optical effects associated with small particles. Singapore: World Scientific; 1988.
[12] Taflove A, Hagness SC. Computational electrodynamics: the finite-difference time-domain method, 2nd ed. Norwood: Artech House; 2000.
[13] Saleh BEA, Teich MC. Fundamentals of photonics. New York: Wiley-Interscience; 1991.
[14] Modest MF. Radiative heat transfer, 2nd ed. San Diego: Academic Press; 2003.
[15] Yariv A. Optical electronics in modern communications, 5th ed. Oxford: Oxford University Press; 1997.
[16] Ohtsu M. Near-field nano-optics: from basic principles to nano-fabrication and nano-photonics. New York: Kluwer/Plenum Publishers; 1999.
[17] Merrifield RB. Solid phase peptide synthesis: I. The synthesis of the tetrapeptide. J Am Chem Soc 1963; 85:2149–54.